RSC Advances

ROYAL SOCIETY OF CHEMISTRY

PAPER

View Article Online
View Journal | View Issue

Check for updates

Cite this: *RSC Adv.*, 2026, **16**, 29350

A mechanically compliant MnO_2–MXene–GelMA cardiac patch for modulating the post-infarction microelectrical environment and alleviating oxidative stress

Meng Han,[a] Hang Jin,[b] Jinhui Zhang,[b] Changrui Zhang,[b] Weihu Yang,*[c] Daoheng Sun*[b] and Wenhua Huang*[a]

Received 16th March 2026
Accepted 12th May 2026

DOI: 10.1039/d6ra02208a

rsc.li/rsc-advances

Conventional cardiac patches are limited by mechanical mismatch, disrupted electrical conduction, and excessive oxidative stress arising from the ischemic microenvironment after myocardial infarction, collectively impairing cardiac repair. Here, we develop a mechanically compliant MnO_2–MXene–GelMA (MMG) cardiac patch designed to regulate the post-infarction microelectrical environment while alleviating oxidative stress. MnO_2-decorated MXene nanosheets were incorporated into a photo-crosslinkable GelMA matrix to generate MMG hydrogels with tunable mechanical and electrical properties. The MMG system operated within a cardiac-matching modulus window and maintained stable electrical functionality under cyclic deformation and bending. *In vitro*, MMG reduced intracellular reactive oxygen species in cardiomyocytes under H_2O_2-induced and oxygen–glucose deprivation conditions. Moreover, MMG supported endothelial cell migration and facilitated Connexin 43-mediated intercellular coupling. This modular strategy integrates structural programmability with functional performance, establishing a multifunctional cardiac patch platform that combines mechanical compliance, microelectrical modulation, and oxidative stress attenuation, and offering a promising direction for minimally invasive cardiac repair.

1. Introduction

Myocardial infarction (MI) leads to irreversible cardiomyocyte loss and initiates maladaptive remodeling that progressively impairs cardiac function.[1] Following ischemic injury, extensive cell death is replaced by fibrotic tissue, resulting in increased myocardial stiffness, disrupted electrical signal propagation, and progressive electromechanical dyssynchrony.[2,3] Meanwhile, sustained oxidative stress associated with ischemia and reperfusion further damages cardiomyocytes, impairs mitochondrial function, and limits endogenous repair.[4] These coupled mechanical, electrical, and redox abnormalities establish a hostile post-infarction microenvironment that hinders functional recovery.

Cardiac patch-based strategies have emerged as a promising approach to support infarcted myocardium and modulate local tissue environments.[5–7] However, the dynamic nature of cardiac contraction imposes stringent requirements on patch design. An ideal patch must mechanically conform to the beating myocardium while restoring disrupted electrical conduction to support synchronous excitation–contraction coupling.[8,9] Increasing evidence further highlights oxidative stress as a key regulator of cardiomyocyte survival and repair, underscoring the need for materials capable of simultaneously addressing electrical dysfunction and redox imbalance.[10,11]

In recent years, conductive cardiac patches have been extensively explored to restore the disrupted electrical microenvironment after myocardial infarction, with representative studies demonstrating the benefits of enhanced conductivity and anisotropic electrical integrity for cardiomyocyte function and post-infarction cardiac repair.[10,11] More recently, molecular insights into electrotransduction have further revealed how conductive scaffolds regulate calcium dynamics and excitation–contraction coupling in engineered myocardial tissues.[12] Despite these advances, most existing conductive cardiac patches focus primarily on enhancing electrical signal transmission.[13–15] While improved conductivity can facilitate electrical integration, many conductive systems rely on rigid

---

[a] Guangdong Engineering Research Center for Translation of Medical 3D Printing Application, National Key Discipline of Human Anatomy, School of Basic Medical Sciences, Southern Medical University, Guangzhou 510515, China. E-mail: huangwenhua2009@139.com

[b] Pen-Tung Sah Institute of Micro-Nano Science and Technology, Xiamen University, Xiamen 361102, PR China. E-mail: sundh@xmu.edu.cn

[c] Key Laboratory of Biorheological Science and Technology, Ministry of Education, College of Bioengineering, Chongqing University, Chongqing 400044, PR China. E-mail: yangweihu@cqu.edu.cn

fillers or high filler loadings that increase stiffness and introduce mechanical mismatch.[16,17] Conversely, antioxidative hydrogels designed to scavenge reactive oxygen species (ROS) often lack sufficient electrical functionality.[18] As a result, existing platforms typically address either electrical or oxidative cues in isolation, despite their intertwined roles in post-infarction electromechanical failure.

MXene-based nanomaterials have recently gained attention for bioelectronic applications owing to their high conductivity, two-dimensional morphology, and processability,[19–21] while MnO_2 has been widely explored as a catalytic antioxidant capable of decomposing excessive ROS.[22,23] Furthermore, existing research has highlighted the significance of combining excellent electrical and mechanical properties with structural programmability in order to achieve complex, tissue-adaptive geometries.[24,25] Gelatin methacryloyl (GelMA), a photocrosslinkable and cell-adhesive hydrogel with tunable mechanics, provides a suitable scaffold for cardiac tissue engineering.[26] Integrating these components within a mechanically compliant hydrogel matrix offers an opportunity to couple electrical and redox regulation.

Here, a mechanically compliant MnO_2–MXene–GelMA (MMG) hydrogel cardiac patch is developed to reshape the post-infarction microelectrical environment while alleviating oxidative stress. MnO_2-decorated MXene nanosheets establish conductive pathways and provide catalytic ROS scavenging,[27,28] while the GelMA matrix ensures softness, deformability, and processability compatible with dynamic myocardium.[29] By tuning MnO_2–MXene content, the MMG platform achieves a balanced electromechanical window that preserves conductivity under cyclic deformation without excessive stiffening.

The electromechanical and antioxidative properties of MMG hydrogels are systematically characterized, followed by evaluation of their biological effects on endothelial cells and cardiomyocytes under oxidative and ischemic stress. The influence of the MMG microenvironment on cardiomyocyte electrical coupling, sarcomeric organization, and cell viability is further examined using iPSC-derived cardiomyocytes. This multifunctional strategy integrates mechanical compliance, electrical stabilization, and oxidative stress regulation within a single hydrogel platform, offering a promising direction for post-infarction myocardial repair (Fig. 1).

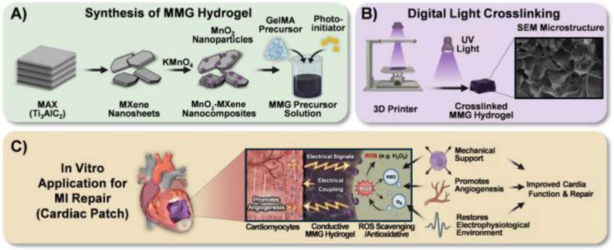

Fig. 1 Schematic illustration of the fabrication, photocrosslinking, and biofunctional roles of the MMG hydrogel. (A) Preparation of MnO_2–MXene nanocomposites and their incorporation into a GelMA precursor. (B) DLP-based photocrosslinking of MMG hydrogels with representative SEM microstructure. (C) Proposed *in vitro* application as a cardiac patch, providing mechanical support, electrical coupling, ROS scavenging, and microenvironmental regulation for myocardial repair.

2. Materials and methods

2.1. Synthesis of MnO_2–MXene nanocomposite

MnO_2–MXene was synthesized in two steps: etching of Ti_3AlC_2 to obtain MXene, followed by *in situ* MnO_2 growth.

First, MXene was prepared by etching Ti_3AlC_2 (Xinxi, China) in a LiF (Macklin, Shanghai, China)/HCl (Lvyin, Xiamen, China) solution at 40–45 °C for 48 h. The product was washed by centrifugation until pH $\approx$ 6, further purified until a dark viscous precipitate formed, and then sonicated in deionized water under inert atmosphere. After centrifugation (3000 rpm, 30 min), a stable MXene colloidal suspension was obtained.

Subsequently, the suspension was mixed with $KMnO_4$ (Hushi, Shanghai, China) and $MnSO_4 \cdot H_2O$ (Hushi, Shanghai, China) in a 6 : 1 molar ratio, followed by addition of concentrated H_2SO_4 (Hushi, Shanghai, China). After stirring for 1 h, the mixture was hydrothermally treated at 140 °C for 24 h. The final product was centrifuged, washed to neutrality, and freeze-dried to yield MnO_2–MXene.

2.2. Preparation of UV curable MnO_2–MXene–GelMA (MMG) hydrogel solutions

The proposed UV-curable MMG hydrogel formula was a mixture of MnO_2–MXene, GelMA, and LAP photoinitiator precursors. The basic hydrogel solution was developed with a composition of GelMA : LAP : DI water = 15 : 1 : 250. The MMG hydrogel solution was prepared at 7 concentrations of MnO_2–MXene (0, 100, 200, 400, 800, 1000, 2000, 5000 μg mL^{-1}). Hereafter, "MMG" followed by a number denotes a specific concentration of the MMG hydrogel. MnO_2–MXene powder was weighed according to the listed concentration and added to the basic hydrogel solution, and then dispersed by ultrasonication overnight. It is worth noting that ultrasound process should be conducted in the dark, and the resulting MMG hydrogel solution should be stored in a refrigerator.

2.3. Characterization of solutions and hydrogels

The morphology of the hydrogels was observed with scanning electron microscope (SEM) (JSM-IT500A, JEOL, Tokyo, Japan).

The rheological properties of the hydrogel precursor were characterized using a rotational rheometer (DHR-20, Waters Corp., USA) at 37 °C. Photocross-linking was initiated by exposing the precursor to a 60 W UV lamp (λ = 405 nm) positioned 5 cm above the sample, yielding an irradiance of approximately 40 mW cm^{-2}.

At room temperature, the mechanical properties of hydrogel samples were measured using an electromechanical universal testing machine (E43, Meters Industrial Systems, USA) at 2 mm min^{-1} with a 50 N load cell. Each sample was tested and recorded with a dial caliper with a precision of 0.02 mm.

The electrical conductivity of solutions of different concentrations was measured using an electrical conductivity meter (DDS-307, LEICI, China).

A bench-top digital multimeter (DMM7510 7 1/2 DIGIT MULTIMETER, Tektronix, USA) was employed to measure and record the direct current resistance changes at both ends of the hydrogel.

The alternating current impedance was measured at room temperature using a three-electrode electrochemical workstation (CHI660E, Chenhua, China). A Pt electrode coated with hydrogel was used as the working electrode, Ag/AgCl was used as the reference electrode, and platinum was used as the counter electrode.

In the measurement of the tensile resistance of the hydrogel, a high-precision displacement platform (XMS50, Newport, France) was used to apply displacement to the hydrogel. A bench-top digital multimeter (DMM7510 7 1/2 DIGIT MULTIMETER, Tektronix, USA) was simultaneously employed to measure and record the resistance changes at both ends of the hydrogel.

2.4. Hydrogel samples manufacturing

The samples were fabricated using a lab-made 3D printer based on digital light processing technology. A 405 nm light source was used, and the light energy density was adjusted to about 250 mW cm^{-2} for our experiments. The 3D digital model was sliced using CHITUBOX V3.2.0, with 50 μm for each layer, corresponding to an exposure time of 6–8 s.

2.5. Cells culture

The HUVECs and H9C2 cell lines were purchased from IMMOCELL (Xiamen, Fujian, China). Cells were grown in an incubator at 37 °C with 5% CO_2 and 95% air. The culture medium was Dulbecco's Modified Eagle Medium (DMEM; Gibco, 11965092), supplemented with 10% sterile fetal bovine serum (FBS; Gibco, 10099141C) and 1% penicillin–streptomycin solution (Gibco, 1719675).

The hiPSC-CMs, exhibiting spontaneous contraction and intrinsic fluorescence, were sourced from Guangdong Yuanxin Regenerative Medicine Co., Ltd. The hiPSCs were labeled with green fluorescent by introducing an EGFP expressional element in an AAVS1 locus. HiPSC-CMs were cultured according to previous publications.[30,31] Prior to cell seeding, all samples were sterilized by γ-irradiation.

2.6. Scratch assay

HUVECs were plated in a 6-well plate and a wound was created in the confluent cell layer using a 200 μL pipette tip. Following the wound, cells were cultured at 37 °C for 24 h. Subsequently, PBS was used to clean and remove the cells that had fallen off due to scraping. The culture medium with 400 μg mL^{-1} concentrations of MMG was added to treat the cells, and the results of cells migration at different treatment times were observed with the fluorescence microscope. ImageJ was used to analyze the wound area.

2.7. *In vitro* oxidative stress assessment

To investigate the protective effect of hydrogels on H9C2 cell apoptosis under oxidative stress, H9C2 cells were seeded in a 24-well plate at a density of 6×10^4 cells per well. The cells in each well were treated with 200 μL of MMG hydrogels at different concentrations (200, 400, 800 μg mL^{-1}) for 12 hours, followed by treatment with 200 μM H_2O_2 for 6 hours. Cell viability was assessed using the CCK-8 assay.

To simulate intracellular oxidative stress, H9C2 cells were seeded in a 6-well plate at a density of 2×10^5 cells per well. The cells in each well were treated with 1 mL of hydrogel for 12 hours, followed by treatment with 200 μM H_2O_2 for additional 6 hours. Intracellular ROS levels were detected using DCFH-DA fluorescent staining (Beyotime, China); fluorescence quantitative analysis of DCFH-DA stained cells was performed using ImageJ.

An *in vitro* OGD model was used to simulate hypoxic injury *in vivo*. Briefly, H9C2 cells were co-cultured with MMG hydrogel in glucose-free DMEM (Gibco, 11966-025) and incubated in a culture incubator (Thermo Fisher Scientific, MA, USA) with an oxygen deprivation bag for 3 hours. The control group was cultured in high-glucose DMEM medium containing 5% CO_2 for the same duration. Intracellular ROS levels were detected using DCFH-DA fluorescent staining while mitochondrial membrane potential was assessed using JC-1 fluorescent staining (Solarbio, China). Mitochondrial polarization was evaluated using JC-1 aggregates (red fluorescence, excitation wavelength 585 nm) and monomers (green fluorescence, excitation wavelength 488 nm).

2.8. Immunostaining and Cx-43 expression

HiPSC-CMs were inoculated in confocal dishes at a density of 4×10^5 cells per well. The experimental group was co-cultured with 500 μL of GelMA/MMG hydrogel for 24 hours. Then the HiPSC-CMs was stained with Cx43 and α-actin.

2.9. Live/dead and viability assay

HiPSC-CMs was inoculated into MMG and cultured for 24 hours. The cell viability was determined by calcitonin/PI staining. Fluorescence quantification of live/dead cells was performed using ImageJ.

2.10. Statistical analysis

The data were indicated by the mean ± standard deviation (SD). Each experimental group conducted at least 3 repetitions of the experiment. We used OriginPro 2024 software for statistical analysis was applied to compare the mean values within each group. Statistical differences were obtained by ANOVA followed by a *post hoc* Tukey's test for significant differences. A significance level of 0.05 was applied to determine significant differences.

2.11. Ethical approval

The cardiomyocytes and endothelial cells used in the study were commercially cells. All cells experiment in the manuscript were approved by the Declaration of Helsinki guidelines.

3. Results and discussion

3.1. Fabrication and physicochemical validation of MMG hydrogels

In summary, the MnO_2–MXene–GelMA (MMG) hydrogel is obtained by uniformly and sonically doping MnO_2–MXene nanofillers into the precursor solution of GelMA hydrogel, and then through 3D additive manufacturing using DLP digital light processing. In this design, MnO_2-decorated MXene nanosheets provide conductive pathways for microelectrical modulation while catalytically scavenging excessive reactive oxygen species, whereas the GelMA matrix offers a soft, photo-crosslinkable scaffold compatible with cyclic myocardial deformation.

The MnO_2–MXene nanofiller was prepared *via* a two-step process: first, Ti_3AlC_2 was subjected to conventional hydrofluoric acid etching to synthesize MXene nanosheets; subsequently, potassium permanganate ($KMnO_4$) and manganese sulfate monohydrate ($MnSO_4 \cdot H_2O$) were introduced as manganese sources, and a redox reaction was initiated under acidic conditions. The resulting product was then collected through centrifugation, followed by freeze-drying to yield the target MnO_2–MXene nanofiller. The nanocomposites exhibited a characteristic nanosheet morphology (Fig. 2B), and energy-dispersive spectroscopy (EDS) together with elemental quantification confirmed successful MnO_2 decoration on MXene surfaces (Fig. 2C, S1 and S2A). The number of Mn atoms is approximately 1.4 times that of Ti atoms. Based on the XPS results of MnO_2–MXene and MXene nanofillers (Fig. 2D), it can be witnessed that the MnO_2–MXene contains four element signals of C 1s, Ti 2p, Mn 2p and O 1s. The XPS profile of Mn 2p (Fig. 2E) can be divided into two sub-peaks, with binding energies of 653.6 and 641.8 eV, corresponding to Mn $2p_{1/2}$ and Mn$2p_{3/2}$, respectively, indicating that the +4 oxidation state of manganese is the predominant form. Fig. S2B shows three fitting peaks of the high-resolution C 1s spectrum, which includes C–Ti (282.0 eV), C–C (284.8 eV) and C═O (288.5 eV). The Ti 2p profile in Fig. S2C confirm the existence of three pairs of bonding: Ti–C (455.3 and 461.4 eV), Ti(II) (462.7 eV), and Ti–O (458.7 and 464.3 eV). In addition, the high-resolution O 1s spectrum (Fig. S2D) discloses the presence of three types of bonds centered at 529.6, 530.7, and 531.7 eV, which are linked to the Ti–O, Mn–O and Ti–OH bonds, respectively. Fig. 2F presents the XRD pattern of the MnO_2–MXene nanofiller. Multiple diffraction peaks are observed, located at 21.5°, 37.0°, 42.2°, 55.6°, corresponding to (120), (131), (300), and (160) of γ-MnO_2 (JCPDS card no. 44-141).

The MMG precursor solutions displayed concentration-dependent pre- and post-photocrosslinking behavior (Fig. 2A) The incorporation of black MnO_2–MXene nanofillers imparts a light-absorbing property to the system, which hinders the photopolymerization process. Specifically, an under-cured phenomenon is observed when the filler concentration exceeds 2000 μg mL^{-1}. The precursor solution (before photopolymerization)'s rheological properties exhibit the same shear-thinning characteristics as GelMA (strain: 1%, angular velocity: 5 rad s^{-1}, Fig. S3B), and remain stable over time, providing a wide processing window for the DLP process with a consistent viscosity (shear rate: 10 s^{-1}, 37 °C, Fig. S3A). Interestingly, as the doping concentration of solid MnO_2–MXene increases, the viscosity of the MMG composite hydrogel precursor shows a decreasing trend. A possible explanation is that the negatively charged MXene surfaces may introduce electrostatic repulsion or shielding effects among GelMA chains,[32] while the abundant oxygen-containing functional groups on MXene and MnO_2 surfaces may form competitive hydrogen bonds with the amide and hydroxyl groups on GelMA, collectively weakening interchain entanglements.[33] Additionally, the two-dimensional nanosheets may act as nano-lubricants, facilitating polymer chain sliding under shear.[34,35] Although the precise mechanism remains to be elucidated, the observed low-viscosity behavior is

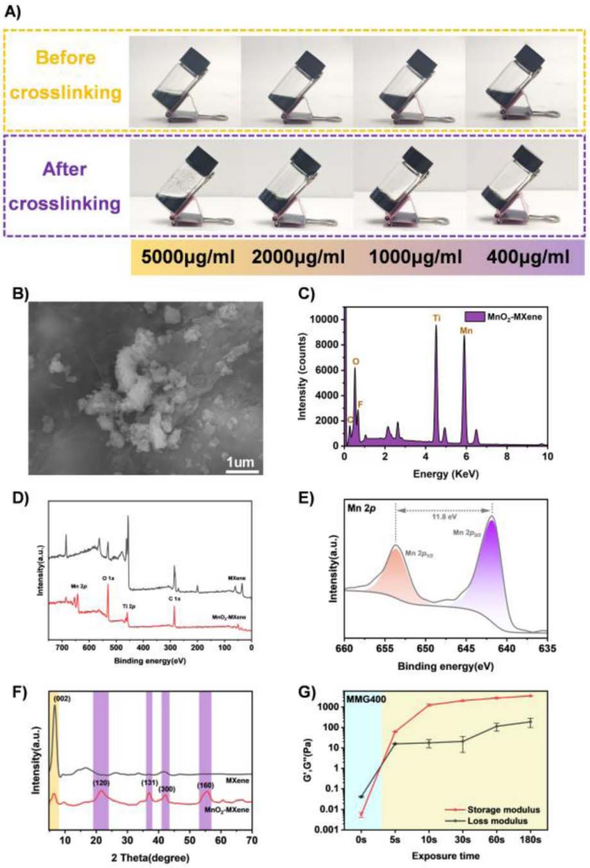

Fig. 2 Synthesis and physicochemical characterization of MnO_2–MXene–GelMA (MMG) hydrogel. (A) MMG precursor solutions before and after photo-crosslinking at different MnO_2–MXene concentrations (400, 1000, 2000, and 5000 μg mL^{-1}). (B) SEM image of MnO_2–MXene nanocomposites. (C) EDS spectrum of MnO_2–MXene. (D) XPS survey spectra of MnO_2–MXene. (E) High-resolution Mn 2p XPS spectra of the MnO_2–MXene sample. (F) XRD patterns of the MnO_2–MXene and MXene samples. (G) Evolution of storage modulus (*G*′) and loss modulus (*G*″) of MMG400 hydrogel during photo-crosslinking.

undoubtedly advantageous for digital light processing (DLP) printing, as it promotes rapid interface rearrangement and smooth detachment of printed parts from the release film.[36,37] The rapid evolution of storage and loss moduli under UV irradiation (Fig. 2G, measured for MMG400) further demonstrates that the MMG composite hydrogel achieves a rapid liquid-to-solid transition within 5 s of UV exposure, highlighting its fast gelation kinetics and compatibility with DLP manufacturing. The SEM images of the lyophilized fully cured hydrogel reveal that the MMG hydrogel maintains substantial voids measuring approximately 40–100 μm (Fig. S4A(i) and (iii)), along with a uniform distribution of MnO_2–MXene particles throughout the porous network (Fig. S4A(ii) and (iv)). EDS and elemental quantitative analysis confirmed the successful modification of the GelMA network (Fig. S4B–D). The observed decrease in Ti and Mn content is attributed to the incorporation of additional hydrogel networks.

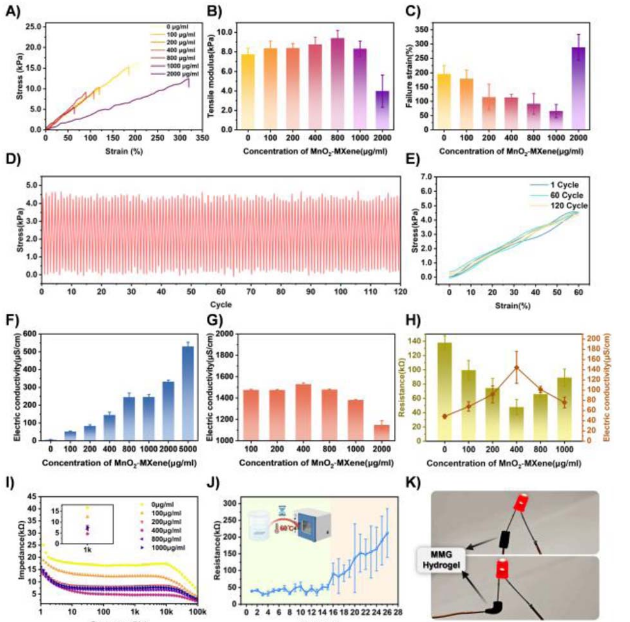

Fig. 3 Mechanical and electrical properties of MMG hydrogels with different MnO_2–MXene concentrations. (A) Tensile curves, (B) elastic modulus, (C) failure strain of MMG with different concentrations. (D) Cyclic compression stress response of MMG hydrogel under repeated loading–unloading cycles. (E) Representative stress–strain hysteresis curves of MMG hydrogel at 1, 60, and 120 compression cycles. (F) Electrical conductivity of MnO_2–MXene aqueous solution. (G) Electrical conductivity of MMG precursor solutions before crosslinking. (H) Electrical resistance and electrical conductivity of crosslinked MMG hydrogels. (I) Alternating current (AC) impedance of crosslinked MMG hydrogels. (J) Curves of resistance of MMG (400 μg mL^{-1}) as a function of time in a solution of pH = 7.4 at 60 °C for simulation. (K) MMG hydrogel maintains stable electrical conductivity under bending conditions.

3.2. Mechanical compliance and fatigue-resilient electromechanical behavior of MMG under cyclic deformation

After establishing the printable window *via* rheological characterization across a broad concentration range, we systematically evaluated the mechanical and electrical properties of the crosslinked solid hydrogels across a finer concentration gradient to identify the optimal formulation for cardiac patch application.

The mechanical properties of photocrosslinked MMG composite hydrogels were evaluated across varying concentrations (Fig. 3A). As the concentration increased, the elastic modulus of the hydrogel exhibited a slight rise, attributed to the MnO_2–MXene nanosheets serving as nanoscale physical crosslinking sites and a rigid reinforcing phase (Fig. 3B). However, once the concentration exceeded 800 μg mL^{-1}, the hydrogel network became incompletely cross-linked due to the light-absorbing effect of MnO_2–MXene, leading to a pronounced decrease in modulus. Regarding failure strain, higher doping concentrations introduced stress concentration within the hydrogel (Fig. 3C), resulting from the modulus mismatch between the rigid MnO_2–MXene nanosheets and the flexible hydrogel matrix. The curing depth of MMG precursor solutions was measured under fixed UV exposure (405 nm, 40 mW cm^{-2}, 300 s). As shown in Fig. S5A, the curing depth decreased progressively with increasing filler concentration: from 8.0 mm for pristine GelMA to 4.7 mm for MMG400, and further to 1.0 mm for MMG2000. According to the Beer–Lambert law[38,39] and the Jacobs working curve,[40,41] the cured region consists of a partially cured part and a fully cured state. The marked decrease in curing depth is directly attributable to the light absorption and scattering by the black MnO_2–MXene nanosheets, which restrict UV penetration. The gel fraction (Fig. S5B) remained stable (∼76–77%) at concentrations ≤ 400 μg mL^{-1}. However, at higher concentrations, it dropped to 73.1% at 800 μg mL^{-1}, 68.9% at 1000 μg mL^{-1}, and 59.8% at 2000 μg mL^{-1}, confirming that excessive nanofiller loading severely impairs the formation of a complete covalent network. Consequently, the fracture strain gradually declined with increasing concentration. When the concentration surpassed 1000 μg mL^{-1}, incomplete cross-linking within the network mitigated stress concentration and hindered crack propagation, thereby enabling the hydrogel to sustain large macroscopic deformations. It is generally believed that a rigid matrix will inhibit the contraction properties of cardiac tissue.[42] Although the modified hydrogel exhibits an increased elastic modulus (9.4 ± 0.8 kPa at 800 μg mL^{-1}), it remains less than that of cardiac tissue (20–500 kPa).[43] Moreover, its fracture strain (65.7% ± 23.2% at 1000 μg mL^{-1}) is sufficient to accommodate the average deformation (∼60%) experienced by cardiac tissue.[44] The uniaxial compression test results of MMG exhibited consistent patterns (Fig. S6A and B). All MMG formulations exhibited compressive modulus below the reported range of native cardiac tissue indicating that the MMG system maintains mechanical compliance even under compression.[45] To evaluate the mechanical stability of the MMG composite hydrogel under prolonged cardiac deformation conditions, cyclic tensile testing was performed. The hydrogel exhibited a stable stress–strain response throughout 120 stretching cycles at 60% strain (Fig. 3D). The hysteresis curves from the 1st, 60th, and 120th cycles were nearly superimposed (Fig. 3E), demonstrating the material's robust mechanical stability under large-strain cyclic loading.

To support micro-electrical remodeling, conductivity was evaluated at three distinct levels: MnO_2–MXene aqueous dispersions, MMG precursor solutions, and crosslinked MMG hydrogels. The dispersion solution of the MnO_2–MXene mixture has measurable electrical conductivity, and its conductivity increases with the increase in concentration (Fig. 3F). This indicates that the MnO_2–MXene composite material can form conductive pathways similar to those of MXene. The incorporation of MnO_2–MXene into the GelMA hydrogel precursor enhanced the electrical conductivity to approximately 1100–1500 $\mu S\ cm^{-1}$ (Fig. 3G), indicating the formation of a dual conductive mechanism involving both ionic and electronic transport within the MMG composite precursor solution. Direct current impedance measurements of the photopolymerized hydrogel (5 mm × 5 mm × 1.5 mm) further corroborated these findings (Fig. 3H). The GelMA hydrogel exhibited a resistance of 137.9 ± 9.8 kΩ and a conductivity of 48.5 ± 3.5 $\mu S\ cm^{-1}$. At a MnO_2–MXene concentration of 400 $\mu g\ mL^{-1}$, the resistance decreased to 47.7 ± 10.6 kΩ, while the conductivity increased 3 times to 144.5 ± 31.2 $\mu S\ cm^{-1}$ (between the conductivity of natural cardiac tissue: 0.05 $mS\ cm^{-1}$ to 1.6 $mS\ cm^{-1}$),[46] indicating the formation of a percolation network within the MMG hydrogel. Upon further increase in MnO_2–MXene content, however, the high surface energy of MnO_2–MXene led to aggregation of the nanofillers. This aggregation hindered their alignment and the establishment of an efficient electronic network, thereby increasing resistance (89.0 ± 12.0 kΩ at 1000 $\mu g\ mL^{-1}$) and reducing conductivity (75.8 ± 10.3 $\mu S\ cm^{-1}$). To evaluate the contribution of each component, we prepared control groups: GelMA/MXene (MxG), GelMA/MnO_2 (MnG), and physically mixed MxMnG (same MnO_2 : MXene ratio as MMG400). As shown in Fig. S7, pristine GelMA and MnG exhibited high resistance (∼130 kΩ), while MxG reduced resistance to 41.2 kΩ. MMG400 achieved nearly uniform resistance (47.7 kΩ), confirming that the *in situ* decorated architecture effectively establishes conductive pathways. The AC impedance of the photopolymerized hydrogels consistently exhibited concentration-dependent conductivity (Fig. 3I). Similar to the trend of the direct current resistance, the MMG hydrogel reached its minimum AC impedance (4.6 kΩ at 1 kHz) at a MnO_2–MXene concentration of 400 $\mu g\ mL^{-1}$. To assess the electrical stability of the MMG composite hydrogels, their aging behavior and electrical properties under cyclic loading were evaluated. The MMG hydrogel was immersed in PBS and aged at 60 °C to accelerate degradation. Resistance began to increase after 15 days (Fig. 3J), attributed to oxidation of MnO_2–MXene and degradation of GelMA. Based on the Arrhenius equation, this failure time can be extrapolated to approximately 74 days under physiological conditions (37 °C).[28] Under both bent and unbent conditions, the MMG hydrogel consistently powered an LED at 5 V (Fig. 3K). Under 20% uniaxial tensile strain, the resistance across the MMG hydrogel was monitored (Fig. S8). Throughout 1000 loading–unloading cycles, the resistance displayed a stable baseline. The change in resistance decreased from 1.55 kΩ initially to 1.02 kΩ at the 1000th cycle. This result indicates that the MMG hydrogel can maintain consistent electrical conductivity under cyclic mechanical deformation, thereby supporting its potential for micro-electrical remodeling during myocardial beating.

3.3. MMG-mediated regulation of endothelial cell migration and cytocompatibility

The cytocompatibility of the MMG hydrogel was first evaluated by culturing H9C2 cardiomyoblasts with extracts from various concentrations of the material. As illustrated in Fig. S9, cell viability exhibited a biphasic trend, initially increasing and then gradually declining at concentrations exceeding 200 $\mu g\ mL^{-1}$. Optimal cell viability was observed at MMG concentrations of 200 and 400 $\mu g\ mL^{-1}$, indicating that the incorporation of MnO_2–MXene within this range does not compromise myocardial biocompatibility. Notably, cell proliferation increased significantly over time, suggesting that the MMG hydrogel provides a safe and effective substrate for supporting cell growth. These findings underscore the potential of MMG for rapid therapeutic applications, particularly in promoting tissue regeneration and the functional recovery of damaged cells without substantial risk of adverse effects.

To further evaluate the reparative potential of the hydrogel, a 2D wound healing (scratch) assay was performed to assess endothelial cell migration (Fig. 4A). To minimize nutritional interference and highlight the intrinsic influence of the MMG microenvironment, the assay was conducted using medium with a low concentration of FBS (1%). Based on the electromechanical optimization established in the previous chapter, the MMG400 formulation was selected to investigate its impact on HUVEC behavior. Fluorescence imaging revealed progressive closure of the scratch area in both the control and MMG groups over time. However, the migration rate in the MMG group was markedly accelerated compared to the control. By 48 h, while the residual scratch area in the GelMA group remained at 15.0% ± 8.9%, the MMG group reached virtually complete closure with a residual area of only 0.5% ± 0.1%, demonstrating the superior capacity of the MMG hydrogel to enhance cellular migration and injury repair (Fig. 4B).

3.4. ROS scavenging and protection against oxidative stress in cardiomyocytes

Beyond supporting cytocompatibility and cell migration, effective myocardial patches are expected to mitigate oxidative stress, a key driver of cardiomyocyte injury in the post-infarction microenvironment. To evaluate the intracellular ROS-scavenging efficacy of the MMG hydrogel, a DCFH-DA fluorescent probe was employed (Fig. 5A).

Compared to the control group, the model group exhibited a pronounced increase in green fluorescence signals following H_2O_2 stimulation, characterized by a widespread and intense fluorescence distribution. This observation signifies a substantial accumulation of intracellular ROS under oxidative stress. In contrast, treatment with MMG hydrogels significantly attenuated the fluorescence intensity in a concentration-dependent manner. Notably, in the MMG400 and MMG800 treatment

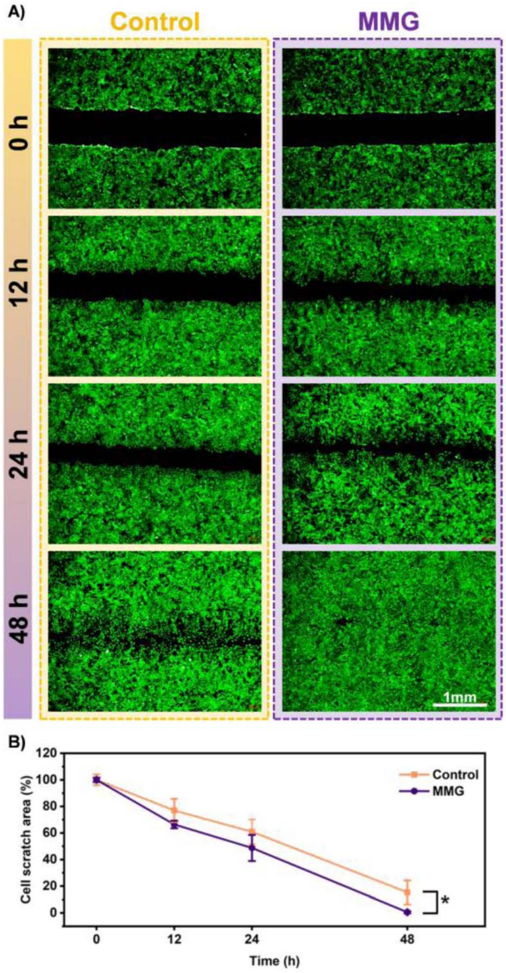

Fig. 4 Effect of MMG hydrogel on cell migration evaluated by scratch assay. (A) Scratch wound healing assay performed on HUVECs, recorded at 0 h, 12 h, 24 h and 48 h. (B) Quantification and analysis of migration area of HUVECs. Data are presented as mean ± SD. *$p <$ 0.05.

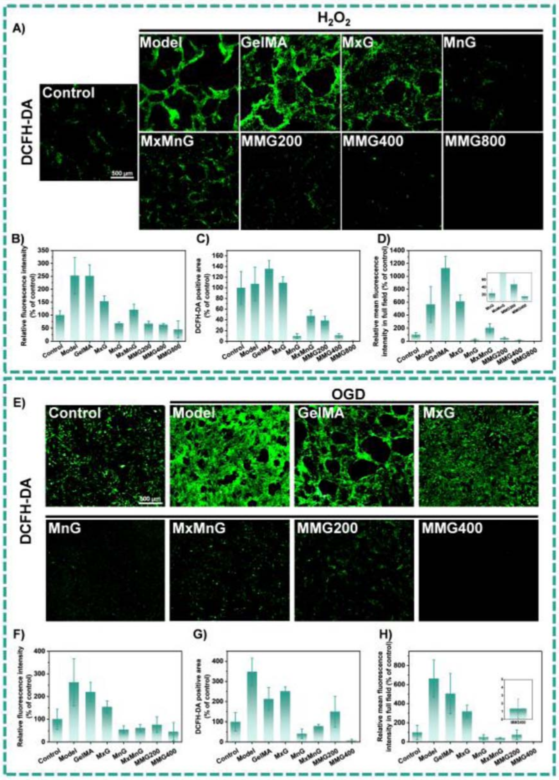

Fig. 5 Intracellular ROS levels in H9C2 cells under oxidative stress conditions. (A) Intracellular ROS levels in H9C2 cells under H_2O_2 stimulation, detected by DCFH-DA staining in the control, model, GelMA, MxG, MnG, MxMnG, and MMG-treated groups. (B–D) Quantification of relative fluorescence intensity, DCFH-DA-positive area, and mean fluorescence intensity in full field of view under H_2O_2 stimulation. (E) Intracellular ROS levels in H9C2 cells under oxygen–glucose deprivation (OGD) conditions, detected by DCFH-DA staining in the control, model, GelMA, MxG, MnG, MxMnG, and MMG-treated groups. (F–H) Quantification of relative fluorescence intensity, DCFH-DA-positive area, and mean fluorescence intensity in full field of view under OGD conditions.

groups, the fluorescence signals were minimal or nearly undetectable, suggesting that the MMG hydrogel effectively neutralizes H_2O_2-induced intracellular ROS.

Quantitative analysis (Fig. 5B–D) further corroborated these qualitative findings. The relative fluorescence intensity of the model group escalated to 252.8% ± 70.9% compared to the control, confirming the successful induction of severe oxidative stress by H_2O_2. Upon intervention with MMG, ROS levels were substantially reduced. Specifically, the relative intensities for the MMG200 and MMG400 groups decreased to 66.2% ± 9.9% and 62.5% ± 5.2%, respectively, with a further reduction to 45.1% ± 32.3% in the MMG800 group. Concomitantly, the ROS-positive area ratio, which reached 107.3% ± 31.2% in the model group, was significantly suppressed to 38.2% ± 8.2%, 10.9% ± 3.6%, and 0.8% ± 0.3% following MMG treatment. Furthermore, analysis of the mean fluorescence intensity throughout the entire field of view revealed that the model group peaked at 563.9% ± 276.8%, while the MMG-treated groups exhibited a drastic decline to 47.7% ± 14.2%, 15.4% ± 4.4%, and 0.9% ± 0.5%. These results collectively demonstrate that the MMG hydrogel not only diminishes the intensity of ROS signals but also significantly constrains their intracellular distribution.

To further assess the cytoprotective effects of MMG under oxidative stress, cell viability was measured using the CCK-8 assay post H_2O_2 stimulation (Fig. S10). The results indicated that the model group's cell viability plummeted to 67.1% ± 23.7%, indicating successful induction of oxidative damage and inhibition of metabolic activity. Treatment with various concentrations of MMG promoted a recovery trend in cell viability. Specifically, the MMG200 and MMG400 groups demonstrated restoration to 103.8% ± 18.5% and 104.2% ± 9.6%, respectively. Interestingly, while the MMG800 group showed a significant improvement compared to the model group (78.9% ± 8.6%), its recovery was less pronounced than that of the medium-concentration groups, exhibiting a non-linear concentration-response characteristic. This suggests that the antioxidant-mediated cytoprotection of the MMG hydrogel operates within a specific therapeutic window, with medium concentrations (MMG200 and MMG400) providing optimal protection by effectively clearing excess ROS while maintaining high cellular metabolic activity. Based on the concentration-dependent protective effects observed in ROS scavenging and cell viability assays (Fig. 5 and S10), MMG200 and MMG400 which exhibited both efficient ROS elimination and high cell viability recovery were selected for further evaluation of mitochondrial membrane potential, while MMG800, despite its strong ROS scavenging activity, showed compromised cell metabolic recovery (Fig. S10) and was therefore excluded from subsequent assays.

A similar protective trend was observed under oxygen–glucose deprivation (OGD) conditions, which more closely simulate the ischemic and hypoxic environment encountered post-myocardial infarction. DCFH-DA staining revealed massive ROS accumulation in the OGD model group (Fig. 5E), with the relative fluorescence intensity rising to 262.6% ± 103.9% and the mean fluorescence intensity throughout the entire field of view reaching 664.1% ± 193.7%, indicating a hypoxia-induced mitochondrial ROS burst. Treatment with MMG significantly suppressed these levels; the relative intensity dropped to 76.3% ± 33.9% in the MMG200 group and further to 45.0% ± 40.1% in the MMG400 group. Moreover, the mean fluorescence intensity in the MMG400 group was reduced to 1.4% ± 1.1%, effectively eliminating high-intensity ROS peaks. Simultaneously, the ROS-positive area ratio was drastically compressed from 348.0% to 7.2% (Fig. 5F–H).

To further dissect the individual and combined contributions of MXene and MnO_2 to ROS scavenging, we additionally evaluated several control formulations under H_2O_2-induced oxidative stress: GelMA, MxG, MnG, and MxMnG. MxG exhibited minimal ROS scavenging activity, while MnG showed moderate reduction of intracellular ROS. The physical mixture (MxMnG) performed better than MxG alone but still inferior to MMG400. A similar trend was observed under oxygen–glucose deprivation (OGD) conditions (Fig. 5E–H). These results demonstrate that the *in situ* decorated (MMG) provides superior ROS scavenging compared to physically mixed counterparts or single components.

Compared to the exogenous H_2O_2 model, OGD better represents the authentic pathological environment of myocardial ischemia. Our findings demonstrate that MMG not only scavenges ROS generated by exogenous oxidative stimuli but also effectively regulates endogenous ROS bursts induced by mitochondrial dysfunction. This underscores the sustained catalytic antioxidant capacity of the MMG hydrogel within pathologically relevant microenvironments.

3.5. Preservation of mitochondrial membrane potential under ischemic stress

Elevated levels of reactive oxygen species (ROS) are known to disrupt mitochondrial membrane potential ($\Delta\Psi_m$), leading to impaired ATP production, inhibited cell proliferation, and the subsequent induction of apoptosis. To evaluate the impact of MMG hydrogels on mitochondrial integrity under pathological conditions, a JC-1 fluorescent probe was utilized to monitor $\Delta\Psi_m$ changes in cells subjected to oxygen–glucose deprivation (OGD).

As illustrated in Fig. 6, the control group exhibited a high red/green fluorescence intensity ratio of 5.5 ± 1.08, indicating that $\Delta\Psi_m$ was well-preserved and mitochondrial health was maintained under normoxic conditions. In sharp contrast, this ratio plummeted to 0.2 ± 0.08 in the OGD model group, signifying severe mitochondrial depolarization and profound organelle dysfunction.

Upon treatment with MMG composite hydrogels, a significant, concentration-dependent restoration of mitochondrial potential was observed. The red/green ratio in the MMG200 group increased to 1.5 ± 0.33. The MMG400 group demonstrated a substantial elevation of the ratio to 4.6 ± 0.67, effectively restoring the $\Delta\Psi_m$ to levels approaching the normoxic control. Correlating these findings with the ROS detection results, it is evident that the OGD-induced endogenous ROS burst is intrinsically linked to mitochondrial depolarization. By significantly attenuating ROS accumulation, MMG400 effectively stabilized $\Delta\Psi_m$, suggesting that its catalytic antioxidant activity successfully disrupts the ROS-mitochondrial damage cascade.

3.6. MMG-mediated enhancement of Cx43 expression and sarcomeric organization in iPSC-CMs

To evaluate the effects of MMG on cardiomyocyte electrical coupling-related protein expression and structural maturation, we analyzed the expression of Connexin 43 (Cx43) and

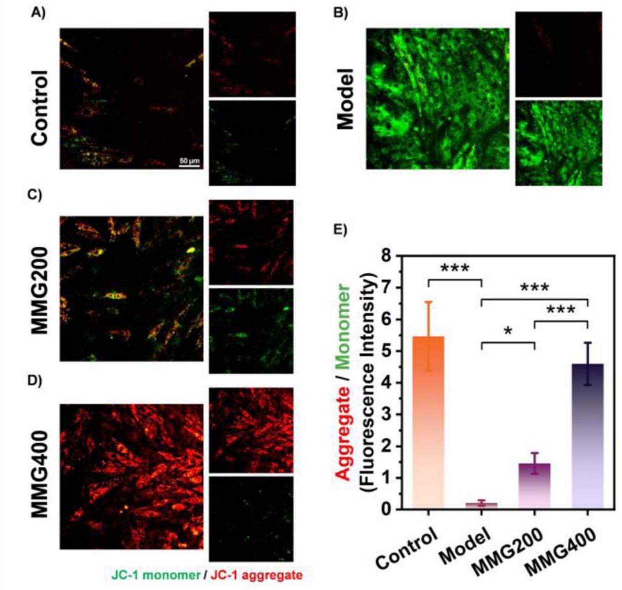

Fig. 6 Mitochondrial membrane potential of H9C2 cells under OGD conditions. (A–D) JC-1 staining of H9C2 cells under OGD conditions. Green fluorescence indicates the monomeric form of JC-1 corresponding to $\Delta\Psi_m$, whereas red fluorescence indicates the aggregated form of JC-1 corresponding to high $\Delta\Psi_m$. (E) Quantification of the JC-1 red/green fluorescence intensity ratio for evaluation of mitochondrial integrity.

sarcomeric organization in iPSC-derived cardiomyocytes (iPSC-CMs) treated with GelMA and MMG hydrogels. MMG400 was selected for Cx43 characterization because it exhibited the most balanced performance across mechanical, electrical, and biological assays. Although MMG200 also showed protective effects on mitochondrial membrane potential, its electrical conductivity was inferior to that of MMG400. Immunofluorescence staining revealed that the expression and intramembrane distribution of Cx43 were significantly enhanced in iPSC-CMs of the MMG group compared to those of the GelMA group (Fig. 7A). Quantitative analysis (Fig. 7B) demonstrated that the area percentage of Cx43 in the GelMA group was merely 3.1% ± 0.97%, whereas it substantially increased to 31.5% ± 15.0% in the MMG group.

As a core structural protein of electrical coupling between cardiomyocytes, the expression level and membrane localization of Cx43 directly determine the propagation efficiency of action potentials between cells. These findings suggest that the MMG composite hydrogel promotes Cx43 expression, a key protein for gap junction formation, which is conducive to improved intercellular communication.

The cytoskeletal structure was further evaluated *via* α-actinin staining. iPSC-CMs treated with MMG exhibited more aligned and well-defined sarcomere structures compared to those with GelMA (Fig. 7C). Quantitative analysis of sarcomere length (Fig. 7D) revealed that the length in the GelMA group was 1.51 ± 0.08 μm, while it significantly increased to 1.74 ± 0.13 μm in the MMG group. Given that the sarcomere length of mature cardiomyocytes typically approaches the 1.70–2.3 μm range,[47–49] the MMG group demonstrated a clear progression toward mature structural characteristics, suggesting enhanced myofibrillar organization and contractile readiness. Such structural improvements are consistent with a microenvironment that simultaneously provides mechanical compliance and stable electrical signaling, both of which are critical for the maturation of cardiomyocytes.

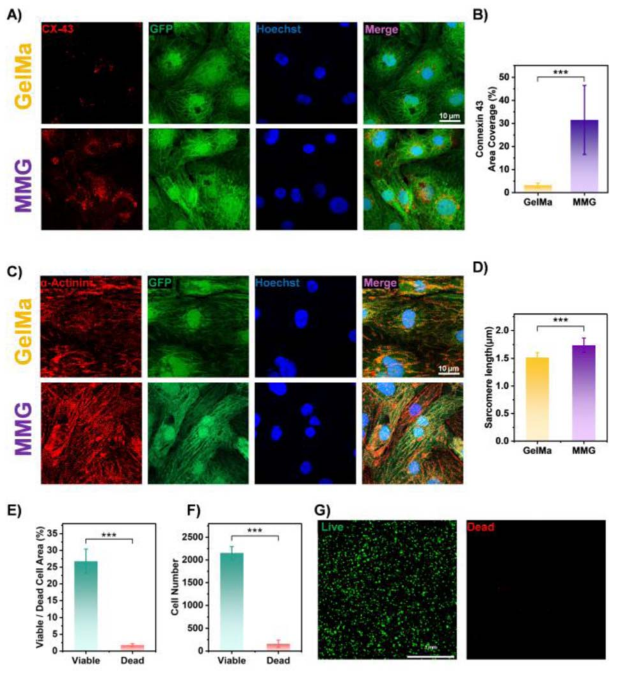

Fig. 7 Connexin 43 expression, sarcomeric organization, and cell viability of iPSC-derived cardiomyocytes treated with GelMA and MMG hydrogels. (A) Cx43 distribution in iPSC-derived cardiomyocytes. (B) Quantitative analysis of Cx43 area coverage in the GelMA and MMG groups. (C) α-Actinin distribution in iPSC-derived cardiomyocytes. (D) Quantification of sarcomere length of iPSC-derived cardiomyocytes. (E) Quantitative analysis of viable and dead cell area percentages. (F) Quantification of viable and dead cell numbers of iPSC-derived cardiomyocytes cultured in MMG hydrogels. (G) Quantification of live and dead cell numbers after 24 h.

3.7. DLP-enabled structured printing of MMG cardiac patches

Finally, to demonstrate manufacturability and geometrical controllability, MMG was patterned *via* DLP printing into a structured patch with 400 μm grooves (Fig. S11), validating that the photocurable MMG precursor supports high-fidelity, structured fabrication relevant to cardiac patch deployment. The cell viability assay further confirmed the biocompatibility of the MMG hydrogel during the printing process. Live/dead staining performed 24 h post-printing revealed that the MMG hydrogel supported a predominantly viable cell population, with only a minimal area of dead cells (Fig. 7G). This observation was corroborated by quantitative cell count analysis (Fig. 7E and F). The high survival rate of iPSC-derived cardiomyocytes on the MMG suggests that the brief ultraviolet exposure and the incorporation of MnO_2–MXene do not induce cytotoxic effects.

4. Conclusion

In this study, we developed a mechanically compliant MnO_2–MXene–GelMA (MMG) hydrogel cardiac patch that integrates electrical modulation and antioxidative capacity to address key pathological features of the post-infarction microenvironment. By embedding MnO_2-decorated MXene nanosheets into a photo-crosslinkable GelMA matrix, the MMG system achieves a balanced electromechanical performance within the physiological range of native myocardium, maintaining stable conductivity under cyclic mechanical loading. *In vitro* studies demonstrated that MMG effectively scavenges intracellular ROS under both H_2O_2-induced and oxygen–glucose deprivation conditions, preserves mitochondrial membrane potential, and supports endothelial cell migration. Furthermore, MMG enhanced Cx43 expression and sarcomeric organization in iPSC-derived cardiomyocytes, suggesting potential for improved electrical coupling and structural maturation. Among the tested formulations, MMG400 exhibited the most balanced performance across mechanical, electrical, and biological assessments. The formulation also exhibited favorable processability for DLP-based 3D printing, enabling the fabrication of structured cardiac patches with high cytocompatibility. Collectively, the MMG hydrogel presents a multifunctional platform that concurrently addresses mechanical compliance, electrical dysfunction, and oxidative stress-three interrelated barriers to cardiac repair. This work offers a promising strategy for the development of next-generation cardiac patches and highlights the potential of integrating nanomaterial-enabled functionality with bioadaptive hydrogel design for minimally invasive myocardial intervention.

Author contributions

M. H. and H. J.: data analysis, investigation, methodology, original draft, conceptualization and formal analysis; M. H., H. J. and J. Z.: experimental part, investigation and methodology; H. J. and J. Z.: data curation; M. H., H. J., J. Z., W. Y. and D. S.: writing – review and editing; M. H. and W. Y.: conceptualization, W. H.: supervision.

Conflicts of interest

There are no conflicts to declare.

Data availability

All data needed to support the conclusions in the paper are present in the paper and the supplementary information (SI). Supplementary information is available. See DOI: https://doi.org/10.1039/d6ra02208a.

Acknowledgements

This research was supported by the National Key R&D Program of China (2022YFB4600600).

Notes and references

1 M. T. Roefs, J. Bauzá-Martinez, S. I. Van De Wakker, J. Qin, W. T. Olijve, R. Tuinte, M. Rozeboom, C. Snijders Blok, E. A. Mol, W. Wu, P. Vader and J. P. G. Sluijter, *Commun. Biol.*, 2023, **6**, 800.

2 H. Esmaeili, A. Patino-Guerrero, M. Hasany, M. O. Ansari, A. Memic, A. Dolatshahi-Pirouz and M. Nikkhah, *Acta Biomater.*, 2022, **139**, 118–140.

3 S. Li, W. Yin, Y. Liu, C. Yang, Z. Zhai, M. Xie, Z. Ye and X. Song, *Biomater. Sci.*, 2025, **13**, 542–567.

4 P. N. Prem and G. A. Kurian, *Heliyon*, 2024, **10**, e31389.

5 M. Shan, Y. Li, L. Wei, W. Li, F. Zhao, F. Wang, Z. Zhang, G. Wang, L. Wang and J. Mao, *Bioact. Mater.*, 2026, **56**, 623–640.

6 Q. Lv, D. Zhou, Y. He, T. Xu, X. Qiu and J. Zeng, *Bioact. Mater.*, 2025, **49**, 172–192.

7 M. Lee, M. C. Kim and J. Y. Lee, *Int. J. Nanomed.*, 2022, **17**, 6181–6200.

8 C. Yu, Z. Yue, M. Shi, L. Jiang, S. Chen, M. Yao, Q. Yu, X. Wu, H. Zhang, F. Yao, C. Wang, H. Sun and J. Li, *ACS Nano*, 2022, **16**, 16234–16248.

9 X. Ren, M. Xiao, Y. Xu, Y. Wu, J. Yang, Y. Wang, Y. Hu, Z. Jiang, X. Li, Z. Shen, S. Hu and M. Tang, *Chem. Eng. J.*, 2024, **481**, 148791.

10 G. Zhao, Y. Feng, L. Xue, M. Cui, Q. Zhang, F. Xu, N. Peng, Z. Jiang, D. Gao and X. Zhang, *Acta Biomater.*, 2022, **139**, 190–203.

11 G. Zhao, X. Zhang, B. Li, G. Huang, F. Xu and X. Zhang, *ACS Biomater. Sci. Eng.*, 2020, **6**, 1630–1640.

12 L. Xue, Q. Zhang, Y. Wang, W. Zhan, M. Cui, N. Peng, Z. Jiang, Z. Xiao and X. Zhang, *Biomaterials*, 2026, **327**, 123712.

13 J. Zhao, Y. Chen, Y. Qin, Y. Li, X. Lu and C. Xie, *Macromol. Rapid Commun.*, 2025, **46**, 2400835.

14 Y. Liao, L. He, Z. Zhang, S. Geng and Q. Ren, *Chem. Eng. J.*, 2025, **525**, 170294.

15 Y. Zhang, A. L. Friec, Z. Zhang, C. A. Müller, T. Du, M. Dong, Y. Liu and M. Chen, *Mater. Today*, 2023, **70**, 237–272.

16 S. H. Lee, J. W. Lee, D. Kim, G. D. Cha and S.-H. Sunwoo, *Gels*, 2025, **11**, 530.

17 F. Xu, H. Jin, L. Liu, Y. Yang, J. Cen, Y. Wu, S. Chen and D. Sun, *Microsyst. Nanoeng.*, 2024, **10**, 96.

18 S. Wang, X. Zhao, Y. Zhan, J. Liang, J. Shi, J. Gu and H. Wang, *Biomacromolecules*, 2025, **26**, 7930–7943.

19 K. N. Alagarsamy, L. R. Saleth, S. Sekaran, L. Fusco, L. G. Delogu, M. Pogorielov, A. Yilmazer and S. Dhingra, *Bioact. Mater.*, 2025, **48**, 583–608.

20 N. Yang, R. Hua, Y. Lai, P. Zhu, J. Ding, X. Ma, G. Yu, Y. Xia, C. Liang, W. Gao, Z. Wang, H. Zhang, L. Yang, K. Zhou and L. Ge, *J. Nanobiotechnol.*, 2025, **23**, 282.

21 L. Bai, Q. Luo, Z. Gao, Y. Wang, Y. Wu, D. Yuan, M. Liu, C. Hu and Y. Wang, *Adv. Funct. Mater.*, 2025, **35**, 10548.

22 L. Chen, P. Cao, P. Zhao, Y. Xu, G. Lv and D. Yu, *Mater. Des.*, 2024, **241**, 112971.

23 H. Gong, J. Zhang, Y. Fan, M. Tian, C. Chen, S. Tan, C. Li, J. Du and S. He, *Adv. Funct. Mater.*, 2026, **36**, e23507.

24 A. Joshi, S. Choudhury, A. Majhi, S. Parasuram, V. S. Baghel, S. Chauhan, S. Khanra, D. Lahiri and K. Chatterjee, *Biomater. Sci.*, 2025, **13**, 4706–4716.

25 S. Choudhury, A. Joshi, V. S. Baghel, G. K. Ananthasuresh, S. Asthana, S. Homer-Vanniasinkam and K. Chatterjee, *J. Mater. Chem. B*, 2024, **12**, 5678–5689.

26 K. Elkhoury, D. Patel, N. Gupta and S. Vijayavenkataraman, *Small*, 2025, **21**, e05968.

27 H. Zheng, F. Cheng, D. Guo, X. He, L. Zhou and Q. Zhang, *Nano Lett.*, 2023, **23**, 7379–7388.

28 F. Wang, F. Liang, Q. Chen, J. Huang, X. Wang, W. Cheng, J. Cui, F. Xu, Y. Mei, X. Wu and E. Song, *Mater. Today Electron.*, 2025, **13**, 100163.

29 J. J. H. M. Smits, A. Van Der Pol, M. J. Goumans, C. V. C. Bouten and I. Jorba, *Front. Bioeng. Biotechnol.*, 2024, **12**, 1363525.

30 B. Lin, X. Lin, M. Stachel, E. Wang, Y. Luo, J. Lader, X. Sun, M. Delmar and L. Bu, *Front. Endocrinol.*, 2017, **8**, 253.

31 L. Liu, F. Xu, H. Jin, B. Qiu, J. Yang, W. Zhang, Q. Gao, B. Lin, S. Chen and D. Sun, *Bioengineering*, 2023, **10**, 702.

32 H. Cho, S. Lim, G. Kim, J. Park, S. Kim, S. Y. Ryu, S. Kang, H. H. Lee and J. Lee, *Colloid Polym. Sci.*, 2023, **301**, 357–370.

33 Z. Bao, N. Bing, X. Zhu, H. Xie and W. Yu, *Chem. Eng. J.*, 2021, **406**, 126390.

34 M. Marian, C. D. Q. Esteban, D. F. Zambrano, S. M. Ramteke, J. R. Grez, B. C. Wyatt, J. Patenaude, B. G. Wright, B. Anasori and A. Rosenkranz, *Appl. Mater. Today*, 2024, **41**, 102464.

35 S. Antony Jose, A. M. Ralls, A. K. Kasar, A. Antonitsch, D. C. Neri, J. Image, K. Meyer, G. Zhang and P. L. Menezes, *Materials*, 2025, **18**, 3927.

36 M. I. Calafel, M. Criado-Gonzalez, R. Aguirresarobe, M. Fernández and C. Mijangos, *Mater. Adv.*, 2025, **6**, 4566–4597.

37 L. Šimunović, L. Brenko, A. J. Marić, S. Meštrović and T. Haramina, *Polymers*, 2025, **17**, 2706.

38 D. F. Swinehart, *J. Chem. Educ.*, 1962, **39**, 333.

39 T. Lee, J.-H. Kim, C. S. Ng, A. Andreu, I. Kim, W. Lee, H. Kim, P.-C. Su and Y.-J. Yoon, *Chem. Eng. J.*, 2024, **482**, 149110.

40 Y. Li, Q. Mao, J. Yin, Y. Wang, J. Fu and Y. Huang, *Addit. Manuf.*, 2021, **37**, 101716.

41 S. Krishnamoorthy, S. Wadnap, B. Noorani, H. Xu and C. Xu, *Eur. Polym. J.*, 2020, **124**, 109487.

42 M. Kharaziha, M. Nikkhah, S.-R. Shin, N. Annabi, N. Masoumi, A. K. Gaharwar, G. Camci-Unal and A. Khademhosseini, *Biomaterials*, 2013, **34**, 6355–6366.

43 M. Kapnisi, C. Mansfield, C. Marijon, A. G. Guex, F. Perbellini, I. Bardi, E. J. Humphrey, J. L. Puetzer, D. Mawad, D. C. Koutsogeorgis, D. J. Stuckey, C. M. Terracciano, S. E. Harding and M. M. Stevens, *Adv. Funct. Mater.*, 2018, **28**, 1800618.

44 L. A. Hidalgo-Bastida, J. J. A. Barry, N. M. Everitt, F. R. A. J. Rose, L. D. Buttery, I. P. Hall, W. C. Claycomb and K. M. Shakesheff, *Acta Biomater.*, 2007, **3**, 457–462.

45 M. Winkelbauer, M. Generali, K. Cheng, M. Y. Emmert and P. Chansoria, *Trends Biotechnol.*, 2026, DOI: 10.1016/j.tibtech.2026.01.014.

46 K. Roshanbinfar, L. Vogt, F. Ruther, J. A. Roether, A. R. Boccaccini and F. B. Engel, *Adv. Funct. Mater.*, 2020, **30**, 1908612.

47 P. P. de Tombe and H. E. D. J. ter Keurs, *J. Mol. Cell. Cardiol.*, 2016, **91**, 148–150.

48 E. I. Rossman, R. M. Berretta, R. E. Petre, K. W. Chaudhary, J. P. Gaughan, S. R. Houser and K. B. Margulies, *J. Card. Failure*, 2003, **9**, S15.

49 P. O. Awinda, Y. Bishaw, M. Watanabe, M. A. Guglin, K. S. Campbell and B. C. W. Tanner, *Br. J. Pharmacol.*, 2020, **177**, 5609–5621.